Check for updates

Geophysical Research Letters

RESEARCH LETTER
10.1029/2026GL122593

Key Points:

- The relative roles and contributions of internal climate variability (ICV) to global surface temperature (GST) uncertainty are evaluated
- Uncertainty in GST due to ICV is primarily driven by contributions from the tropics, in particular, during the SSP5-8.5 period
- Changes in the tropical Pacific and the Gulf Stream mean SST are linked to changes in the contribution of ICV to GST uncertainty

Supporting Information:

Supporting Information may be found in the online version of this article.

Correspondence to:

S.-W. Yeh,
swyeh@ewha.ac.kr

Citation:

Oh, S.-Y., Yeh, S.-W., & Kirtman, B. P. (2026). Diagnosis of the contribution of internal climate variability to global surface temperature projection under future warming. *Geophysical Research Letters*, *53*, e2026GL122593. https://doi.org/10.1029/2026GL122593

Received 25 FEB 2026
Accepted 15 APR 2026

Author Contributions:

Conceptualization: Sae-Yoon Oh, Sang-Wook Yeh, Benjamin P. Kirtman
Formal analysis: Sae-Yoon Oh
Investigation: Sae-Yoon Oh
Methodology: Sae-Yoon Oh
Supervision: Sang-Wook Yeh
Validation: Sae-Yoon Oh
Writing – original draft: Sae-Yoon Oh
Writing – review & editing: Sang-Wook Yeh, Benjamin P. Kirtman

© 2026. The Author(s).
This is an open access article under the terms of the Creative Commons Attribution-NonCommercial-NoDerivs License, which permits use and distribution in any medium, provided the original work is properly cited, the use is non-commercial and no modifications or adaptations are made.

Diagnosis of the Contribution of Internal Climate Variability to Global Surface Temperature Projection Under Future Warming

Sae-Yoon Oh[1], Sang-Wook Yeh[1], and Benjamin P. Kirtman[2]

[1]Department of Climate and Energy Systems Engineering, Ewha Womans University, Seoul, South Korea, [2]Rosenstiel School for Marine, Atmospheric, and Earth Science, University of Miami, Miami, FL, USA

Abstract Internal climate variability (ICV) is a critical source of uncertainty in global surface temperature (GST) projections. We find regional drivers of ICV in GST projections and investigate their evolution under anthropogenic forcing. Among four CMIP6 large ensemble simulations under historical and SSP5-8.5 scenarios, we focus on MIROC6 and CanESM5, which show contrasting behaviors of ICV related to GST. In MIROC6, ICV, quantified by ensemble variance, increases markedly from the historical to the future period, primarily driven by the tropical variability including El Niño-Southern Oscillation (ENSO). Conversely, CanESM5 exhibits stable ICV from the historical to the future period. In CanESM5, while both ENSO and Barents-Kara Sea ice are key drivers in the historical period, ENSO dominates in the future. These contrasts are associated with forced mean-state changes in tropical Pacific and North Atlantic sea surface temperature.

Plain Language Summary Climate's natural variability provides an irreducible range for future global surface temperature (GST) projections, making its understanding crucial for risk assessment and decision-making. Using CMIP6 models, we show that the GST projection range due to internal climate variability is not consistent under future warming. We then focus on two models under the same scenario but exhibiting contrasting behaviors. In one model, the GST range grows significantly, driven by enhanced sea surface temperature (SST) variability in the central-to-eastern tropical Pacific. In the other model, however, the range remains stable as increasing tropical SST variability is offset by decreasing Arctic variability from Barents-Kara Sea ice loss. These divergences align with background state shifts, including weakened equatorial SST gradients and North Atlantic warming. Accurately representing both tropical and Arctic processes is essential for reliable GST projections.

1. Introduction

Internal climate variability (ICV) is a fundamental uncertainty source in global surface temperature (GST) projections, significantly modifying near-future GST changes (Deser et al., 2012; Hawkins & Sutton, 2009; Maher et al., 2020). While aggregate ICV contributions to GST uncertainty are extensively quantified (Hawkins & Sutton, 2009; Lehner et al., 2020; Maher et al., 2020), accurately disentangling specific drivers to the GST projections related to ICV remains poorly elucidated, which is essential for addressing non-stationary ICV under anthropogenic forcing and improving the reliability of future climate projections (Lehner & Deser, 2023).

Recent advances in Large Ensemble (LE) simulations enable separating ICV from externally driven climate change (Blanusa et al., 2023; Haszpra, Herein, & Bódai, 2020; Maher et al., 2020). These simulations reveal that drivers of ICV can be active on decadal scales (Deser et al., 2016, 2020; Lehner & Deser, 2023), often masking or amplifying forced responses (Dai & Bloecker, 2019; Rodgers et al., 2021). While ICV dominates short-term changes and remains important for medium-term projections (Deser et al., 2016; Lehner & Deser, 2023; Maher et al., 2020), whether future ICV in GST projections will increase or decrease, and which specific drivers underpin this change, have not been comprehensively assessed. Some studies leveraging LE simulations have identified the Arctic and the tropical Pacific as the primary regions driving ICV (Coquereau et al., 2024; Olonscheck et al., 2021). They highlight that future warming leads to divergent regional trends, specifically, decreasing ICV in the Arctic due to Barents Sea ice loss and increasing ICV in the Tropics linked to ENSO. However, how these contrasting evolutions collectively determine ICV related to GST remains poorly

19448007, 2026, 10, Downloaded from https://agupubs.onlinelibrary.wiley.com/doi/10.1029/2026GL122593 by Ewha Womans University Library, Wiley Online Library on [21/09/2026]. See the Terms and Conditions (https://onlinelibrary.wiley.com/terms-and-conditions) on Wiley Online Library for rules of use; OA articles are governed by the applicable Creative Commons License

Table 1
List of Large Ensembles Used in This Study

Model	Resolution (lon × lat) (atm/ocn)	Simulation years	Initialization method	Number of ensemble members	Forcing	Climate sensitivity	References
ACCESS-ESM1-5	1.9° × 1.3°/1° × 1°	1850–2100	Macro	40	Historical, SSP5-8.5	3.9K	Ziehn et al. (2020)
CanESM5	2.8° × 2.8°/1° × 1°	1850–2100	Macro	25	Historical, SSP5-8.5	5.6K	Swart et al. (2019)
MIROC6	1.4° × 1.4°/1° × 1°	1850–2100	Macro	50	Historical, SSP5-8.5	2.6K	Shiogama et al. (2023); Tatebe et al. (2019)
MPI-ESM1-2-LR	1.9° × 1.9°/ 1.5° × 1.5°	1850–2100	Macro	30	Historical, SSP5-8.5	2.8K	Mauritsen et al. (2019); Müller et al. (2018)

understood. Furthermore, systematic evaluations are lacking on how the evolving interplay between these drivers leads to divergent behaviors across models.

This study evaluates the spatiotemporal evolution of ICV related to GST using four Coupled Model Intercomparison Project Phase 6 (CMIP6) LE simulations under the historical and SSP5-8.5 scenarios. We investigate transient spatial patterns of surface temperature variability that contribute most to ICV related to GST using snapshot empirical orthogonal function (SEOF) analysis, which calculates EOF across the ensemble dimension instead of the time dimension, thereby allowing us to obtain contemporaneous modes of variability without forced trends (Haszpra, Topal, & Herein, 2020; Haszpra, Herein, & Bodai, 2020; Maher et al., 2018). By examining how background state changes modulate ICV drivers, in addition, we aim to refine the characterization of ICV's role in GST projections, which is a crucial step for informing robust climate mitigation and adaptation strategies.

2. Data and Methods

2.1. Large Ensemble Model Data Sets

We analyze four CMIP6 LEs (1850–2100), selected for their sufficient ensemble size to robustly separate ICV from forced signals (Table 1). Simulations follow historical (1850–2014) and high-emission SSP5-8.5 (2015–2100), which provides a strong forcing to examine changes in drivers of ICV (Eyring et al., 2016). To sample the full range of internal variability, each ensemble member of the historical simulations in all models is initialized from a different state of a long pre-industrial control simulation (macro-initialization method).

Variables include annual mean surface air temperature (SAT), sea surface temperature (SST), and sea ice concentration (SIC). GST is calculated as the area-weighted global average of SAT, while SST and SIC are used to evaluate the impacts of ENSO (Niño-3.4) and Barents-Kara Seas (BKS) ice variability on ICV in GST projection. Annual means are defined from June to May to maintain the physical continuity of the boreal winter (December-January-February) and the peak ENSO phase (Deser et al., 2012) without artificial calendar-year truncation.

2.2. Quantifying ICV in GST Projections

This study focuses on GST projection attributable to ICV, which is quantified by the ensemble variance of annual GST anomalies following previous studies (Blanusa et al., 2023; Coquereau et al., 2024; Lehner et al., 2020). We apply additive decomposition of the total GST variance into regional contributions from the Tropics (30°S–30°N), Northern Hemisphere (NH; 30°–90°N), and Southern Hemisphere (SH; 30°–90°S). Following weighted sum variance properties, decomposition is expressed as:

$$\mathrm{Var}_e(\mathrm{GST}) = \sum_i w_i^2 \mathrm{Var}_e(T_i) + \sum_{i \neq j} w_i w_j \mathrm{Cov}_e(T_i, T_j) \quad (1)$$

where w_i is the area-weighting factor, T_i is the regional mean SAT, and $\mathrm{Var}_e(x)$ and $\mathrm{Cov}_e(x, y)$ is the variance and covariance computed in the ensemble dimension e. Each shaded area in Figure 2c represents the contribution of a specific region, accounting for its weighted variance and the shared covariance with other regions, ensuring the sum of all components equals the total ICV in GST projection. One may consider the influence of initialization

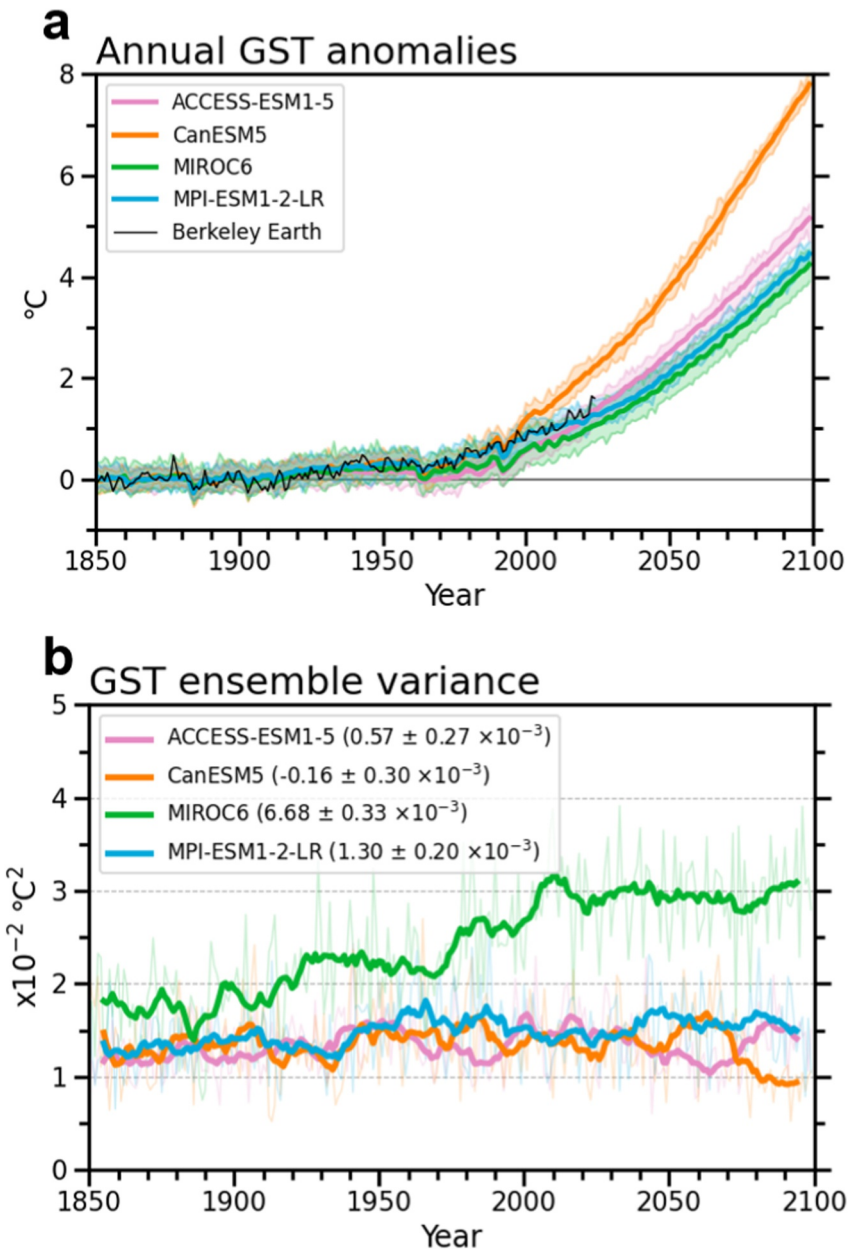


Figure 1. (a) Annual global surface temperature (GST) anomalies (1850–1900 baseline) and (b) GST ensemble variance. (a) Thick lines and shading denote ensemble means and min-max spreads for ACCESS-ESM1-5 (pink), CanESM5 (orange), MIROC6 (green), and MPI-ESM1-2-LR (blue). Black line shows Berkeley Earth observations (Rohde & Hausfather, 2020). (b) Thin and thick lines indicate annual and decadal running mean ensemble variance. Legend in (b) reports linear trends in decadal variance with 95% confidence intervals.

methodologies to generate ensemble members (Deser et al., 2025; Shiogama et al., 2023; Swart et al., 2019). All models utilize macro-initialization, branching from diverse pre-industrial control simulations, ensuring that inter-model spread reflects regional physical mechanisms rather than initialization techniques.

2.3. Snapshot EOF (SEOF) Analysis

For each year, SAT deviations were calculated by subtracting the ensemble mean from each individual member to isolate ICV. We apply snapshot EOF (SEOF) analysis to the global SAT deviations across the ensemble members for each year. Unlike traditional EOF analysis, which identifies patterns over time, SEOF performs EOF analysis

19448007, 2026, 10, Downloaded from https://agupubs.onlinelibrary.wiley.com/doi/10.1029/2026GL122593 by Ewha Womans University Library, Wiley Online Library on [21/09/2026]. See the Terms and Conditions (https://onlinelibrary.wiley.com/terms-and-conditions) on Wiley Online Library for rules of use; OA articles are governed by the applicable Creative Commons License

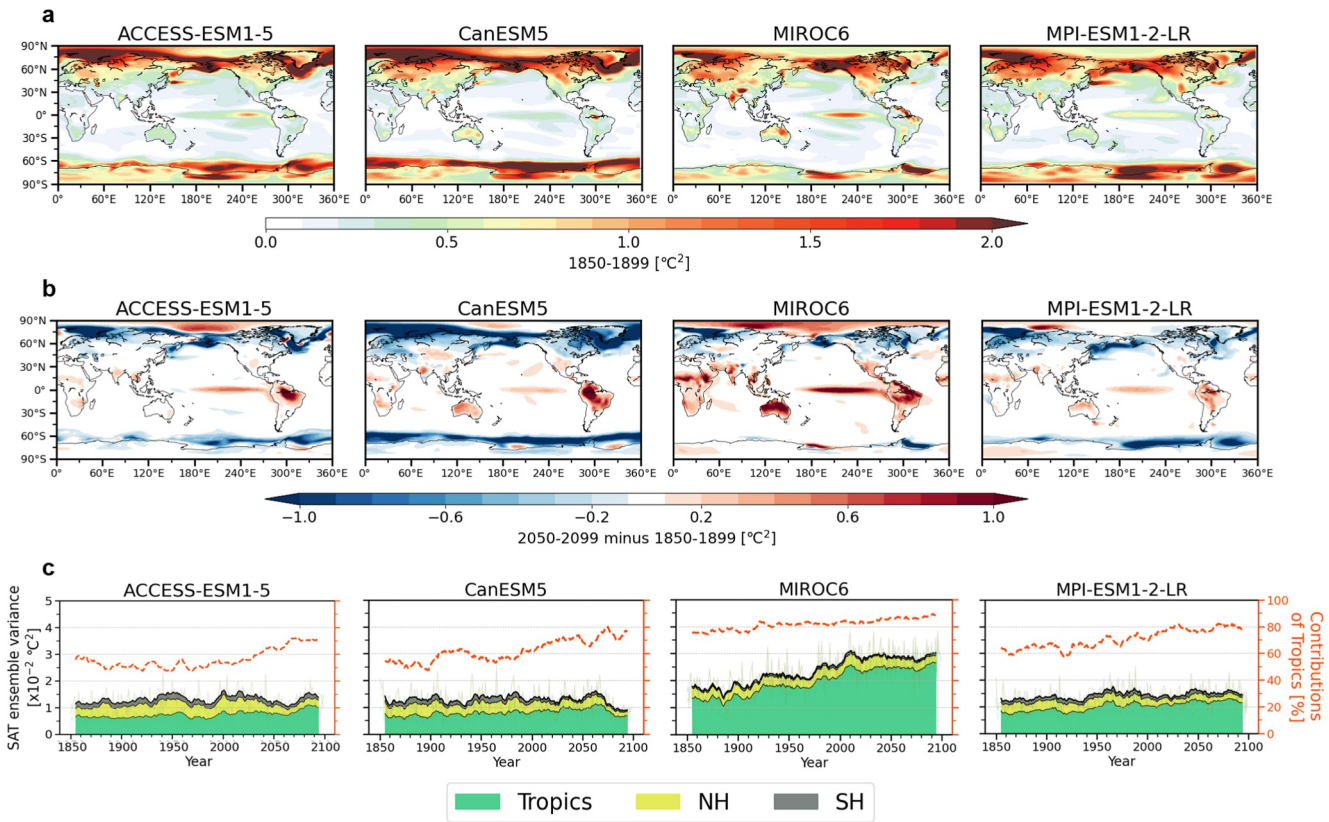


Figure 2. (a) Surface air temperature (SAT) ensemble variance (1850–1899) and (b) its projected changes for 2050–2099. (c) Decomposition of GST ensemble variance into Tropics (30°S–30°N; green), Northern Hemisphere (NH; 30°–90°N; yellow), and Southern Hemisphere (SH; 90°–30°S; gray). Orange dashed line (right axis) denotes the fractional tropical contribution. Thin and thick lines indicate annual and decadal means, respectively.

on the ensemble dimension at each discrete annual time step, capturing instantaneous ICV modes (Haszpra, Topal, & Herein, 2020; Haszpra, Herein, & Bodai, 2020). The leading SEOF1 pattern represents the dominant spatial structure of the driver of ICV for each year, tracing its spatiotemporal evolution throughout the simulation period (O'Brien & Deser, 2023).

3. Results

3.1. Changes in ICV of GST Projection and Latitudinal Contributions

We first examine the historical trajectories of annual GST anomalies relative to the 1850–1900 baseline across the four LEs (Figure 1a). While all models capture the observed climatological spatial characteristics with high fidelity (Figure S1 in Supporting Information S1), their forced responses exhibit divergent trajectories, reflecting model-specific climate sensitivities and physics (thick lines in Figure 1a and Table 1). Despite these divergent forced signals, the magnitude of ICV in GST is generally well-represented across these models, without systematic over- or underestimation relative to observations (Suarez-Gutierrez et al., 2021). Within each LE simulation, individual ensemble members deviate from the ensemble mean GST for a given year. These deviations arise from differences in ICV within the same external forcing and the same climate system in each LE simulation. ICV generates a non-negligible level of uncertainty, exceeding 0.5°C, as reflected by the range between the maximum and minimum GST across ensemble members (Figure 1a). ICV at each discrete time step is typically quantified by using ensemble variance (or standard deviation) (Blanusa et al., 2023; Coquereau et al., 2024; Lehner et al., 2020; Maher et al., 2020).

Figure 1b presents the temporal evolution of ICV, quantified as the ensemble variance of annual GST, over 1850–2100. MIROC6 displays the most prominent increase, indicating an intensified ICV contribution under warming. MPI-ESM1-2-LR and ACCESS-ESM1-5 show similar but less pronounced increasing trends, while

19448007, 2026, 10, Downloaded from https://agupubs.onlinelibrary.wiley.com/doi/10.1029/2026GL122593 by Ewha Womans University Library, Wiley Online Library on [21/09/2026]. See the Terms and Conditions (https://onlinelibrary.wiley.com/terms-and-conditions) on Wiley Online Library for rules of use; OA articles are governed by the applicable Creative Commons License

19448007, 2026, 10, Downloaded from https://agupubs.onlinelibrary.wiley.com/doi/10.1029/2026GL122593 by Ewha Womans University Library, Wiley Online Library on [21/09/2026]. See the Terms and Conditions (https://onlinelibrary.wiley.com/terms-and-conditions) on Wiley Online Library for rules of use; OA articles are governed by the applicable Creative Commons License

CanESM5 remains relatively stable. These divergent trajectories suggest that the response of ICV to identical radiative forcing is model-dependent.

To further understand different trends of ICV in GST projection, we examine the spatial pattern of SAT ensemble variance for the pre-industrial period (1850–1899) and its projected change for the late 21st century (2050–2099) in each LE (Figures 2a and 2b). During 1850–1900, two regions dominate ICV across all models. High latitudes exhibit the largest variability, especially over the Antarctic and the Arctic seas, including BKS (Figure 2a). These features show good agreement with observations (Figure S2 in Supporting Information S1). ACCESS-ESM1-5 and CanESM5 also show high variability over the North Atlantic. Additionally, the Tropics, particularly the tropical Pacific, show large SAT variability, with MIROC6 displaying the largest variability for the pre-industrial period.

Under intensified radiative forcing, high-latitude SAT variability generally declines, although parts of the Arctic show localized increases (Figure 2b). SAT variability in high latitudes for CanESM5 and ACCESS-ESM1-5 decreases more rapidly during 2050–2099 compared to other LEs. Meanwhile, the SAT variability in low latitudes increases in all models, most notably in MIROC6. These opposing changes—declining high-latitude and increasing low-latitude variability—align with previous studies and are linked to Arctic sea-ice loss and ENSO intensification (Coquereau et al., 2024; Olonscheck et al., 2021).

To assess latitudinal contribution of different drivers of ICV, the GST ensemble variance is decomposed into the Tropics (30°S–30°N), Northern Hemisphere (NH; 30°–90°N), and Southern Hemisphere (SH; 30°–90°S) (Figure 2c). The Tropics yield the largest share of GST variability due to their expansive area and spatially coherent variability. In MIROC6, the fractional contribution of the Tropics increases from 80% during the historical period to nearly 90% by the late 21st century, primarily driving the marked rise in ICV in GST projection (Figure 2c, orange dashed line). NH contributions (≈20%–45% during the historical period) are secondary and decline in future projections. In CanESM5, ACCESS-ESM1-5, and MPI-ESM1-2-LR, rising low-latitude variability is largely offset by high-latitude decreases, resulting in stable ICV related to GST throughout the 21st century.

3.2. Temporal Evolution of ICV Drivers Contributing to GST Projection

To identify evolving ICV drivers, we apply SEOF analysis (1850–2099) to grid-point SAT deviations from the ensemble mean across the global domain. As SEOF is performed across the member axis, the leading SEOF1 pattern provides a snapshot of the dominant driver of ICV contributing to instantaneous GST variability each year, which allows the dominant mode to vary annually and enables a more precise characterization of its spatiotemporal evolution throughout the simulation period (Haszpra, Topal, & Herein, 2020; Haszpra, Herein, & Bodai, 2020; Maher et al., 2018; O'Brien & Deser, 2023). Hereafter, we focus on two LEs that exhibit contrasting behaviors with regard to ICV related to GST from historical to future periods. The first is MIROC6, which shows a marked increase during the historical period (Figure 2c). The second is CanESM5, which remains stable throughout the simulation period (Figure 2c). Note that the results for MPI-ESM1-2-LR and ACCESS-ESM1-5 are consistent with MIROC6 and CanESM5, respectively, particularly regarding the spatial patterns and evolution of the SEOF1 mode.

We examine the evolution of SEOF1 during the historical period. In MIROC6, SEOF1 in 1850 ($SEOF1_{1850}$, hereafter) manifests as an ENSO-like temperature pattern explaining 23% of GST variability (Figure 3a). This structure represents coherent ICV-driven SAT deviation, not individual ENSO events, and it indicates that ENSO-related drivers dominate GST variability. In contrast, $SEOF1_{1850}$ in CanESM5 shows both the ENSO-like pattern and a large variance in the BKS, accounting for 17% explained variance. When the SSP5-8.5 scenario forcing starts, both MIROC6 and CanESM5 show the ENSO-like pattern in SEOF1 in 2015 ($SEOF1_{2015}$, hereafter) (Figures 3b and 3d).

To evaluate how this leading SEOF evolves with time, we calculate annual pattern correlations with $SEOF1_{1850}$ for 1850–2099 and $SEOF1_{2015}$ for 2015–2099 (Figures 3e and 3f). In MIROC6, pattern correlations remain above 0.8 for the entire historical and SSP5-8.5 period, indicating that ENSO-related SAT variability consistently serves as the dominant source of ICV related to GST (Figure 3e). Unlike MIROC6, CanESM5 exhibits low and scattered correlations with $SEOF1_{1850}$ during the historical period (Figure 3f). These inconsistent patterns are due to the multiple dominant drivers of ICV related to GST in CanESM5, which are linked to ENSO and BKS variability in CanESM5 (Figure S3 in Supporting Information S1). However, during the SSP5-8.5 period, correlations with

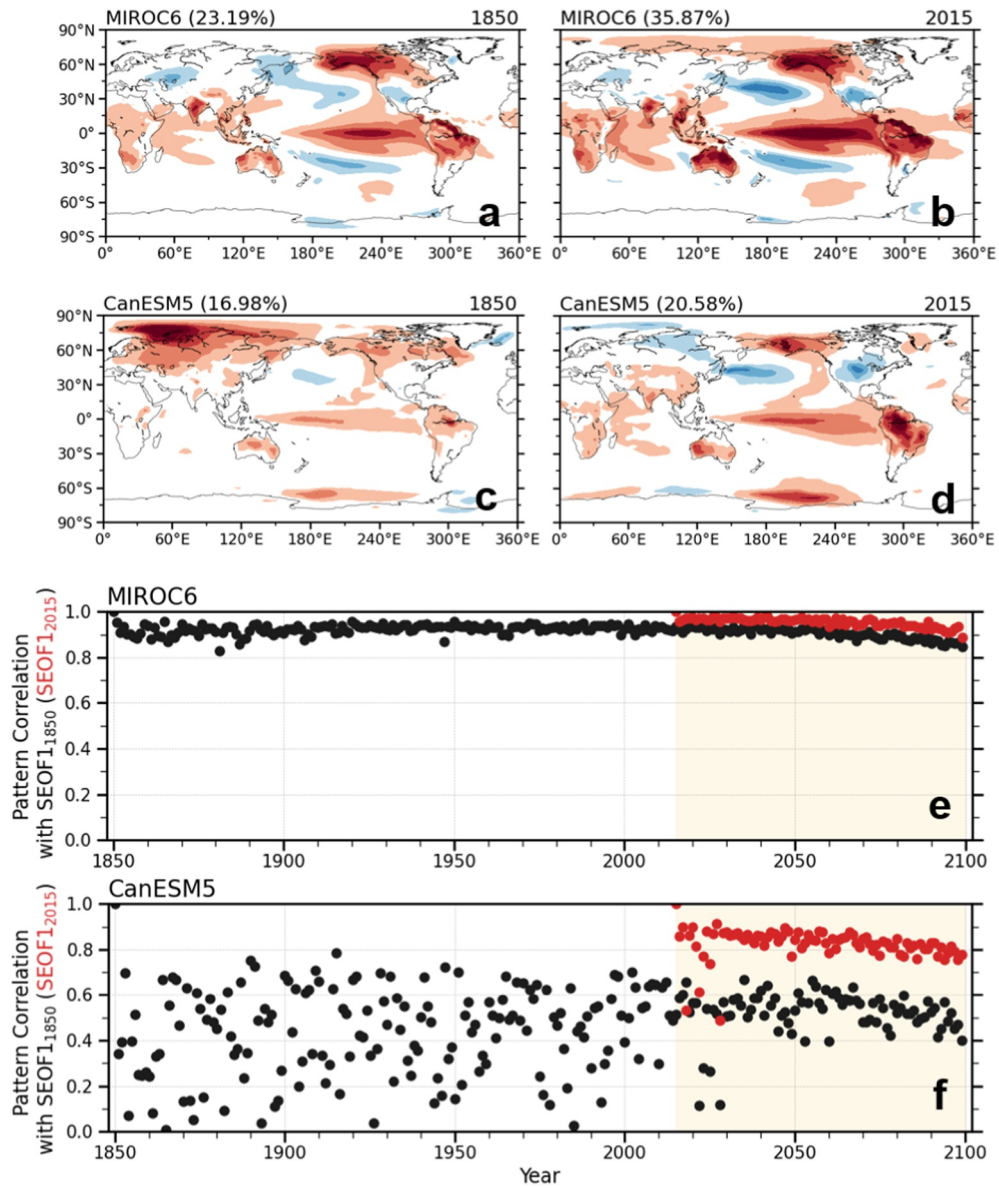


Figure 3. Snapshot EOF (SEOF) leading patterns in 1850 (SEOF1$_{1850}$) and 2015 (SEOF1$_{2015}$) for (a, b) MIROC6 and (c, d) CanESM5. Annual SEOF1 pattern correlation coefficients with SEOF1$_{1850}$ (black) and SEOF1$_{2015}$ (red; 2015–2099 under SSP5-8.5) for (e) MIROC6 and (f) CanESM5.

SEOF1$_{2015}$ remain high in CanESM5. This indicates that the influence of BKS weakens and ENSO emerges as the dominant driver of GST ensemble variance in CanESM5.

To examine the fidelity of the simulated internal variability, we compared the characteristics of ENSO and BKS-SIC against ERA5 reanalysis (Figures S4 and S5 in Supporting Information S1). Both MIROC6 and CanESM5 capture the characteristic ENSO spatial structures, linear trend of BKS-SIC, and the relationship between BKS-SIC and North Atlantic SST. However, variability magnitudes differ. MIROC6 overestimates the 30-year running variance of Niño-3.4 SST, while CanESM5 aligns closer to ERA5 despite a slight underestimation. Conversely, CanESM5 overestimates BKS-SIC variability, whereas MIROC6 more closely follows observations. These regional biases underpin the divergent GST trajectories related to ICV, highlighting that MIROC6's overestimation of ENSO variability likely overstates the magnitude of the projected increase in future ICV, whereas CanESM5's overestimation of BKS-SIC variability yields a stable ICV projection as the rapid decline in Arctic variability offsets tropical increases.

19448007, 2026, 10, Downloaded from https://agupubs.onlinelibrary.wiley.com/doi/10.1029/2026GL122593 by Ewha Womans University Library, Wiley Online Library on [21/09/2026]. See the Terms and Conditions (https://onlinelibrary.wiley.com/terms-and-conditions) on Wiley Online Library for rules of use; OA articles are governed by the applicable Creative Commons License

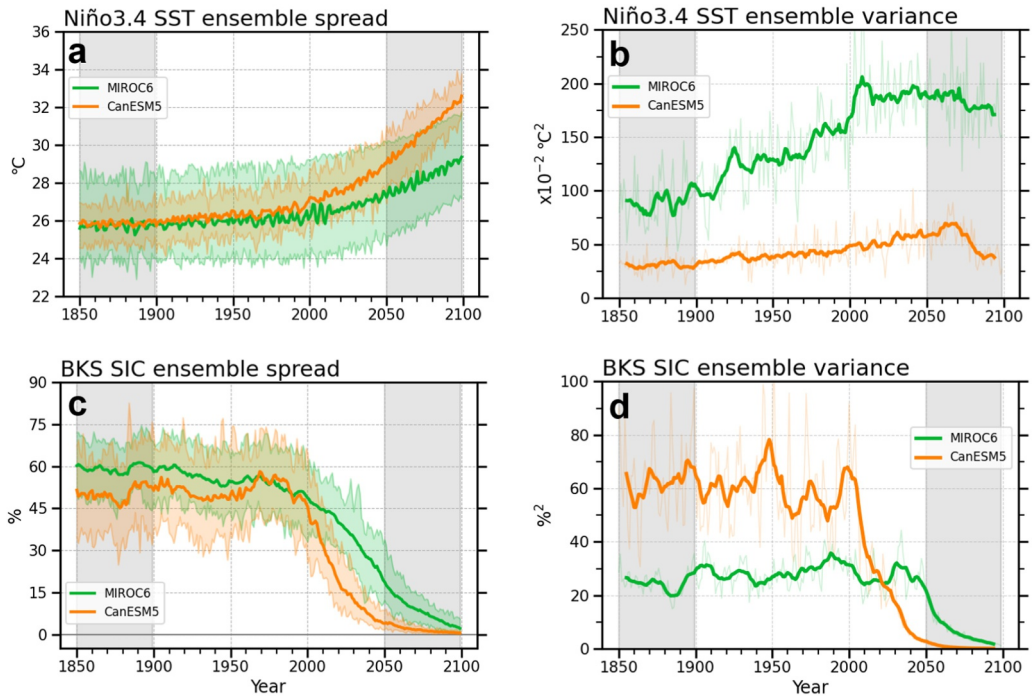


Figure 4. Same as Figure 1 but for (a, b) annual sea surface temperature (SST) in the Niño-3.4 region (5°S–5°N, 170°–120°W) and (c, d) annual sea ice concentration (SIC) over the BKS region (65°–85°N, 20°–90°E). Gray shading represents the 1850–1899 and 2050–2099 periods.

3.3. Impacts of Changing Background State on Drivers of ICV

To understand how ENSO and BKS-SIC influence ICV in GST projection in both models, we examine the SST variability in the central-to-eastern equatorial Pacific (Niño-3.4 region; 5°S–5°N, 170°–120°W) and SIC variability over the BKS (65°–85°N, 20°–90°E).

Figures 4a and 4b show the ensemble spread of annual SST in the Niño-3.4 region and its annual and decadal ensemble variance for MIROC6 and CanESM5. Although the ensemble-mean Niño-3.4 SST is similar between the two models during 1850–1899, MIROC6 exhibits a larger SST ensemble spread that increases more strongly toward 2099. Notably, the correlation between the decadal running ensemble variance of Niño-3.4 SST (Figure 4b) and GST (Figure 1b) is $r = 0.98$ in MIROC6 ($p < 0.01$) for the entire 1850–2099 period, suggesting tropical SST as the primary driver of its ICV related to GST. In contrast, the correlation is only $r = 0.30$ in CanESM5 ($p < 0.01$). Instead, CanESM5 shows larger BKS-SIC variability during 1850–1899, which then declines rapidly during 2050–2099 due to accelerated sea-ice loss (Figures 4c and 4d). These divergent trajectories likely reflect each model's unique representation of pre-industrial ICV and distinct responses to greenhouse gas-induced changes in the background state.

We assess how future changes in the tropical Pacific SST background modulate ENSO variability. When the equatorial zonal SST gradient weakens, deep convection and westerly wind anomalies extend eastward, strengthening the Bjerknes feedback and increasing ENSO amplitude (Fredriksen et al., 2020; Lee et al., 2022; Maher et al., 2023; Zheng et al., 2016). MIROC6 exhibits an ensemble-mean weakening of the zonal SST gradient, defined as the west Pacific (5°S–5°N, 120°–180°E) minus the east Pacific (5°S–5°N, 150°–90°W) annual-mean SST difference, by −0.9°C from 1850 to 1899 to 2050–2099, which is roughly twice the reduction in CanESM5 (Figure 5a). This more pronounced background change aligns with a stronger increase in Niño-3.4 SST variability for MIROC6. Across members, zonal SST gradient changes are linearly associated with changes in Niño-3.4 SST variability (Figure 5b), estimated as 50-year running variances of annual SST deviations from the ensemble mean.

For BKS-SIC, surface warming in the North Atlantic (30°–50°N, 80°–30°W) acts as a key pacemaker of sea-ice decline (Jung et al., 2017; Kumar et al., 2021; Sato et al., 2014; Yamagami et al., 2022). Warmer North Atlantic

19448007, 2026, 10, Downloaded from https://agupubs.onlinelibrary.wiley.com/doi/10.1029/2026GL122593 by Ewha Womans University Library, Wiley Online Library on [21/09/2026]. See the Terms and Conditions (https://onlinelibrary.wiley.com/terms-and-conditions) on Wiley Online Library for rules of use; OA articles are governed by the applicable Creative Commons License

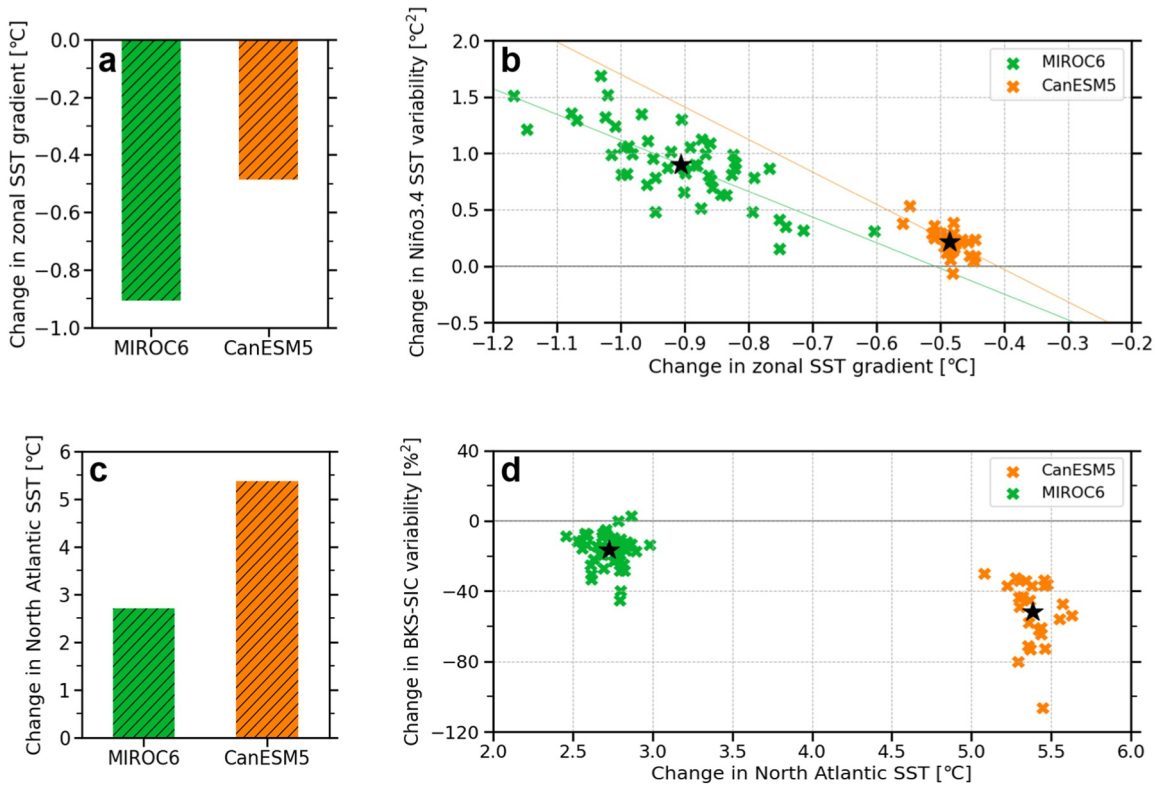


Figure 5. (a) Ensemble-mean equatorial zonal SST gradient change (2050–2099 minus 1850–1899) for MIROC6 (green) and CanESM5 (orange). The gradient is West (5°S–5°N, 120°–180°E) minus East (5°S–5°N, 150°–90°W) annual-mean SST. Hatching indicates 95% significance. (b) Scatter plot of zonal SST gradient change (*x* axis; 2050–2099 minus 1850–1899) versus Niño-3.4 variability change (*y* axis) for individual ensemble members (crosses) and ensemble mean (stars). (c) Same as (a), but for the North Atlantic (30°–50°N, 80°–30°W) SST change. (d) Same as (b), but for the change in North Atlantic SST (*x* axis) versus BKS-SIC variability (*y* axis).

SSTs intensify northward ocean heat transport and upper-ocean heat content in the BKS, accelerating sea-ice loss and reducing BKS-SIC variability. Compared to MIROC6, CanESM5 exhibits faster North Atlantic warming (Figure 5c), consistent with its more rapid reduction in BKS-SIC variability. Indeed, most CanESM5 members show stronger North Atlantic warming and greater BKS-SIC variability reductions than MIROC6 (Figure 5d), indicating that faster North Atlantic SST warming in CanESM5 drives greater sea-ice loss and, consequently, larger changes (i.e., decrease) in BKS SIC variability.

4. Conclusion and Discussion

This study demonstrates that ICV in GST projections is non-stationary, changing significantly from the historical to the SSP5-8.5 periods. In MIROC6, ICV increases markedly due to amplified ENSO-related variability under increasing greenhouse-gas forcing. Conversely, CanESM5 exhibits stable ICV, as rising tropical signals are offset by declining high-latitude variability. To robustly identify these drivers, we employed SEOF analysis, as it is specifically designed to evaluate the non-stationary internal variability that arises under anthropogenic forcing (Haszpra, Topal, & Herein, 2020; Haszpra, Herein, & Bodai, 2020; Maher et al., 2018). We found that during the historical period, ENSO-related SAT variability is the dominant contributor to GST variability in MIROC6, whereas both ENSO and BKS-SIC variability are important in CanESM5. However, under SSP5-8.5, ENSO emerges as the dominant driver in both models. Since SSP5-8.5 imposes the strongest forcing, the magnitude and timing of this emerging ENSO dominance should be considered an upper bound, and may be weaker and/or delayed in lower-emission scenarios. Mechanistically, MIROC6's larger increase in Niño-3.4 SST variability is linked to a more pronounced weakening of the equatorial zonal SST gradient. In CanESM5, greater North Atlantic SST warming accelerates BKS-SIC loss, rapidly reducing its variability.

To refine future GST projections, ICV should be treated as a non-stationary source under strong anthropogenic forcing and depending on the model. Our results show that the ICV related to GST is shaped by the transient

19448007, 2026, 10, Downloaded from https://agupubs.onlinelibrary.wiley.com/doi/10.1029/2026GL122593 by Ewha Womans University Library, Wiley Online Library on [21/09/2026]. See the Terms and Conditions (https://onlinelibrary.wiley.com/terms-and-conditions) on Wiley Online Library for rules of use; OA articles are governed by the applicable Creative Commons License

interplay, specifically the compensation or reinforcement, between regional drivers like ENSO and Arctic sea ice. Consistency across other LEs, including MPI-ESM1-2-LR and ACCESS-ESM1-5, confirms the robustness of the identified mechanisms (Figures S6–S8 in Supporting Information S1). Identifying how the interplay determines the divergent ICV emphasizes the importance of evaluating underlying physical mechanisms for robust climate risk assessments.

Conflict of Interest

The authors declare no conflicts of interest relevant to this study.

Availability Statement

Large Ensemble data sets (ACCESS-ESM1-5, CanESM5, MIROC6, and MPI-ESM1-2-LR) are retrieved from ESGF nodes (https://esgf-metagrid.cloud.dkrz.de/search/ and https://aims2.llnl.gov/search/cmip6/). ERA5 near-surface temperature is available at https://cds.climate.copernicus.eu/datasets/reanalysis-era5-single-levels-monthly-means?tab=download, and Berkeley Earth Surface Temperature is obtained at http://berkeleyearth.org/data/. Code and preprocessed data used for the analysis in this paper are available at Zenodo via Oh et al. (2026).

Acknowledgments
This work is funded by the Korea Meteorological Administration Research and Development Program (Grant RS-2025-02313090).

References

Blanusa, M. L., López-Zurita, C. J., & Rasp, S. (2023). Internal variability plays a dominant role in global climate projections of temperature and precipitation extremes. *Climate Dynamics*, *61*(3–4), 1–15. https://doi.org/10.1007/s00382-023-06664-3

Coquereau, A., Sévellec, F., Huck, T., Hirschi, J. J.-M., & Hochet, A. (2024). Anthropogenic changes of interannual-to-decadal climate variability in CMIP6 multi-ensemble simulations. *Journal of Climate*, *37*(14), 3723–3739. https://doi.org/10.1175/JCLI-D-23-0606.1

Dai, A., & Bloecker, C. E. (2019). Impacts of internal variability on temperature and precipitation trends in large ensemble simulations by two climate models. *Climate Dynamics*, *52*(1), 289–306. https://doi.org/10.1007/s00382-018-4132-4

Deser, C., Kim, W. M., Wills, R. C., Simpson, I. R., Yeager, S., Danabasoglu, G., et al. (2025). Effects of macro vs. micro initialization and ocean initial-condition memory on the evolution of ensemble spread in the CESM2 large ensemble. *Climate Dynamics*, *63*(1), 62. https://doi.org/10.1007/s00382-024-07553-z

Deser, C., Lehner, F., Rodgers, K. B., Ault, T., Delworth, T. L., DiNezio, P. N., et al. (2020). Insights from Earth system model initial-condition large ensembles and future prospects. *Nature Climate Change*, *10*(4), 277–286. https://doi.org/10.1038/s41558-020-0854-5

Deser, C., Phillips, A., Bourdette, V., & Teng, H. (2012). Uncertainty in climate change projections: The role of internal variability. *Climate Dynamics*, *38*(3–4), 527–546. https://doi.org/10.1007/s00382-010-0977-x

Deser, C., Terray, L., & Phillips, A. S. (2016). Forced and internal components of winter air temperature trends over North America during the past 50 years: Mechanisms and implications. *Journal of Climate*, *29*(6), 2237–2258. https://doi.org/10.1175/JCLI-D-15-0304.1

Eyring, V., Bony, S., Meehl, G. A., Senior, C. A., Stevens, B., Stouffer, R. J., & Taylor, K. E. (2016). Overview of the coupled model intercomparison project phase 6 (CMIP6) experimental design and organization. *Geoscientific Model Development*, *9*(5), 1937–1958. https://doi.org/10.5194/gmd-9-1937-2016

Fredriksen, H. B., Berner, J., Subramanian, A. C., & Capotondi, A. (2020). How does El Niño–southern oscillation change under global warming—A first look at CMIP6. *Geophysical Research Letters*, *47*(22), e2020GL090640. https://doi.org/10.1029/2020GL090640

Haszpra, T., Herein, M., & Bódai, T. (2020). Investigating ENSO and its teleconnections under climate change in an ensemble view–A new perspective. *Earth System Dynamics*, *11*(1), 267–280. https://doi.org/10.5194/esd-11-267-2020

Haszpra, T., Topál, D., & Herein, M. (2020). On the time evolution of the Arctic oscillation and related wintertime phenomena under different forcing scenarios in an ensemble approach. *Journal of Climate*, *33*(8), 3107–3124. https://doi.org/10.1175/JCLI-D-19-0004.1

Hawkins, E., & Sutton, R. (2009). The potential to narrow uncertainty in regional climate predictions. *Bulletin of the American Meteorological Society*, *90*(8), 1095–1108. https://doi.org/10.1175/2009BAMS2607.1

Jung, O., Sung, M.-K., Sato, K., Lim, Y.-K., Kim, S.-J., Baek, E.-H., et al. (2017). How does the SST variability over the western North Atlantic Ocean control Arctic warming over the Barents–Kara Seas? *Environmental Research Letters*, *12*(3), 034021. https://doi.org/10.1088/1748-9326/aa5f3b

Kumar, A., Yadav, J., & Mohan, R. (2021). Spatio-temporal change and variability of Barents-Kara sea ice, in the Arctic: Ocean and atmospheric implications. *The Science of the Total Environment*, *753*, 142046. https://doi.org/10.1016/j.scitotenv.2020.142046

Lee, S., L'Heureux, M., Wittenberg, A. T., Seager, R., O'Gorman, P. A., & Johnson, N. C. (2022). On the future zonal contrasts of equatorial Pacific climate: Perspectives from Observations, Simulations, and Theories. *npj Climate and Atmospheric Science*, *5*(1), 82. https://doi.org/10.1038/s41612-022-00301-2

Lehner, F., & Deser, C. (2023). Origin, importance, and predictive limits of internal climate variability. *Environmental Research: Climate*, *2*(2), 023001. https://doi.org/10.1088/2752-5295/accf30

Lehner, F., Deser, C., Maher, N., Marotzke, J., Fischer, E. M., Brunner, L., et al. (2020). Partitioning climate projection uncertainty with multiple large ensembles and CMIP5/6. *Earth System Dynamics*, *11*(2), 491–508. https://doi.org/10.5194/esd-11-491-2020

Maher, N., Lehner, F., & Marotzke, J. (2020). Quantifying the role of internal variability in the temperature we expect to observe in the coming decades. *Environmental Research Letters*, *15*(5), 054014. https://doi.org/10.1088/1748-9326/ab7d02

Maher, N., Matei, D., Milinski, S., & Marotzke, J. (2018). ENSO change in climate projections: Forced response or internal variability? *Geophysical Research Letters*, *45*(20), 11390–11398. https://doi.org/10.1029/2018GL079764

Maher, N., Wills, R. C. J., DiNezio, P., Klavans, J., Milinski, S., Sanchez, S. C., et al. (2023). The future of the El Niño–Southern oscillation: Using large ensembles to illuminate time-varying responses and inter-model differences. *Earth System Dynamics*, *14*(2), 413–431. https://doi.org/10.5194/esd-14-413-2023

19448007, 2026, 10, Downloaded from https://agupubs.onlinelibrary.wiley.com/doi/10.1029/2026GL122593 by Ewha Womans University Library, Wiley Online Library on [21/09/2026]. See the Terms and Conditions (https://onlinelibrary.wiley.com/terms-and-conditions) on Wiley Online Library for rules of use; OA articles are governed by the applicable Creative Commons License

Mauritsen, T., Bader, J., Becker, T., Behrens, J., Bittner, M., Brokopf, R., et al. (2019). Developments in the MPI-M Earth system model version 1.2 (MPI-ESM1. 2) and its response to increasing CO2. *Journal of Advances in Modeling Earth Systems*, *11*(4), 998–1038. https://doi.org/10.1029/2018MS001400

Müller, W. A., Jungclaus, J. H., Mauritsen, T., Baehr, J., Bittner, M., Budich, R., et al. (2018). A higher-resolution version of the max Planck institute Earth system model (MPI-ESM1. 2-HR). *Journal of Advances in Modeling Earth Systems*, *10*(7), 1383–1413. https://doi.org/10.1029/2017MS001217

O'Brien, J. P., & Deser, C. (2023). Quantifying and understanding forced changes to unforced modes of atmospheric circulation variability over the North Pacific in a coupled model large ensemble. *Journal of Climate*, *36*(1), 19–37. https://doi.org/10.1175/JCLI-D-22-0101.1

Oh, S.-Y., Yeh, S.-W., & Kirtman, B. P. (2026). ICV-GST-Projections: Code for analyzing ICV contributions to GST projections (v1.0.0). *Zenodo*. https://doi.org/10.5281/zenodo.19456453

Olonscheck, D., Schurer, A. P., Lücke, L., & Hegerl, G. C. (2021). Large-scale emergence of regional changes in year-to-year temperature variability by the end of the 21st century. *Nature Communications*, *12*(1), 7237. https://doi.org/10.1038/s41467-021-27515-x

Rodgers, K. B., Lee, S.-S., Rosenbloom, N., Timmermann, A., Danabasoglu, G., Deser, C., et al. (2021). Ubiquity of human-induced changes in climate variability. *Earth System Dynamics*, *12*(4), 1393–1411. https://doi.org/10.5194/esd-12-1393-2021

Rohde, R. A., & Hausfather, Z. (2020). The Berkeley Earth land/ocean temperature record. *Earth System Science Data Discussions*, *2020*(4), 1–16. https://doi.org/10.5194/essd-12-3469-2020

Sato, K., Inoue, J., & Watanabe, M. (2014). Influence of the gulf stream on the Barents Sea ice retreat and Eurasian coldness during early winter. *Environmental Research Letters*, *9*(8), 084009. https://doi.org/10.1088/1748-9326/9/8/084009

Shiogama, H., Tatebe, H., Hayashi, M., Abe, M., Arai, M., Koyama, H., et al. (2023). MIROC6 large ensemble (MIROC6-LE): Experimental design and initial analyses. *Earth System Dynamics Discussions*, *2023*(6), 1–28. https://doi.org/10.5194/esd-14-1107-2023

Suarez-Gutierrez, L., Milinski, S., & Maher, N. (2021). Exploiting large ensembles for a better yet simpler climate model evaluation. *Climate Dynamics*, *57*(9), 2557–2580. https://doi.org/10.1007/s00382-021-05821-w

Swart, N. C., Cole, J. N., Kharin, V. V., Lazare, M., Scinocca, J. F., Gillett, N. P., et al. (2019). The Canadian Earth system model version 5 (CanESM5. 0.3). *Geoscientific Model Development*, *12*(11), 4823–4873. https://doi.org/10.5194/gmd-12-4823-2019

Tatebe, H., Ogura, T., Nitta, T., Komuro, Y., Ogochi, K., Takemura, T., et al. (2019). Description and basic evaluation of simulated mean state, internal variability, and climate sensitivity in MIROC6. *Geoscientific Model Development*, *12*(7), 2727–2765. https://doi.org/10.5194/gmd-12-2727-2019

Yamagami, Y., Watanabe, M., Mori, M., & Ono, J. (2022). Barents-Kara sea-ice decline attributed to surface warming in the Gulf Stream. *Nature Communications*, *13*(1), 3767. https://doi.org/10.1038/s41467-022-31117-6

Zheng, X.-T., Xie, S.-P., Lv, L.-H., & Zhou, Z.-Q. (2016). Intermodel uncertainty in ENSO amplitude change tied to Pacific Ocean warming pattern. *Journal of Climate*, *29*(20), 7265–7279. https://doi.org/10.1175/JCLI-D-16-0039.1

Ziehn, T., Chamberlain, M. A., Law, R. M., Lenton, A., Bodman, R. W., Dix, M., et al. (2020). The Australian Earth system model: ACCESS-ESM1. 5. *Journal of Southern Hemisphere Earth Systems Science*, *70*(1), 193–214. https://doi.org/10.1071/ES19035

19448007, 2026, 10, Downloaded from https://agupubs.onlinelibrary.wiley.com/doi/10.1029/2026GL122593 by Ewha Womans University Library, Wiley Online Library on [21/09/2026]. See the Terms and Conditions (https://onlinelibrary.wiley.com/terms-and-conditions) on Wiley Online Library for rules of use; OA articles are governed by the applicable Creative Commons License